Received: 28 February 2020 | Revised: 10 April 2021 | Accepted: 13 April 2021

DOI: 10.1002/eqe.3467

RESEARCH ARTICLE

WILEY

Dynamic calibration and seismic validation of numerical models of URM buildings through permanent monitoring data

Serena Cattari[1] | **Stefania Degli Abbati**[1] | **Sara Alfano**[1] | **Andrea Brunelli**[1] | **Filippo Lorenzoni**[2] | **Francesca da Porto**[2]

[1] Department of Civil, Chemical and Environmental Engineering, University of Genoa, Genoa, Italy

[2] Department of Geosciences, University of Padua, Padua, Italy

Correspondence
S. Degli Abbati, Department of Civil, Chemical and Environmental Engineering, University of Genoa, Via Montallegro 1, 16145 Genoa, Italy.
Email: stefania.degliabbati@unige.it

Abstract

The construction of reliable numerical models is a key aspect within the seismic assessment of existing unreinforced masonry buildings. However, it is also a complex process due to the many uncertainties involved that can affect the structural response. In situ tests allow for the acquisition of data at a local scale. Nonetheless, supplementary information representing the global response is necessary to overcome other uncertainties (i.e., wall-to-wall connections or floor stiffness). To this end, data from ambient vibration tests (AVT) are useful to support seismic assessments. In fact, they allow for the identification of dynamic structural properties, which are useful in refining the calibration of numerical models. In addition, they address solutions for the aforementioned uncertainties. In this context, the paper presents how to efficiently exploit AVT data by using the case study of the former Courthouse of Fabriano (Ancona, Marche). This structure has been monitored since 2010 by the Italian Department of Civil Protection with a network of 28 seismic accelerometers. As a result, the equivalent frame (EF) model was calibrated in the linear field thanks to the dynamic identification provided under operational conditions. Subsequently, nonlinear dynamic analyses were performed using the recordings acquired during the Central Italy earthquake in 2016/2017. Even if the building experienced only a slight nonlinear behaviour, this comparison between the simulated and actual seismic response made it possible to validate the EF model, especially with reference to the capability in reproducing the amplification phenomena, which is extremely important for the assessment of structural and non-structural components.

KEYWORDS

dynamic identification, equivalent frame models, masonry structures, permanent monitoring, recordings from seismic events

1 | INTRODUCTION

A crucial aspect in the seismic assessment process of unreinforced masonry (URM) structures is the design of reliable numerical models able to accurately simulate natural seismic behaviour.

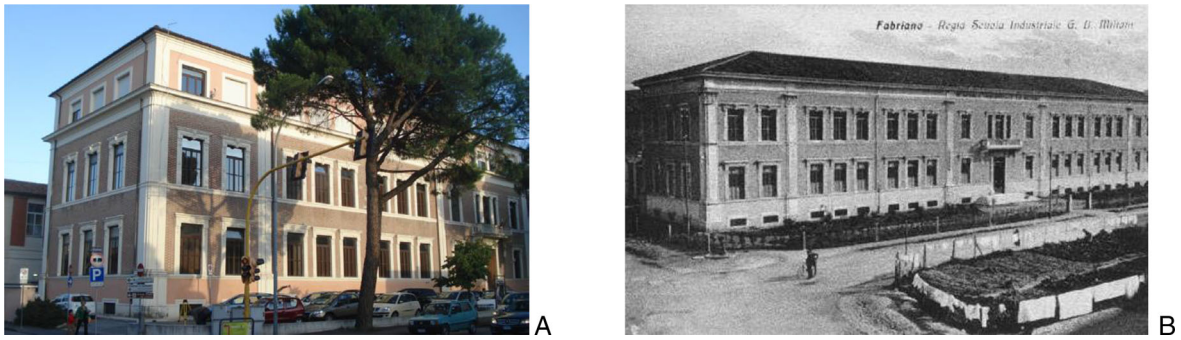

FIGURE 1 (A) A recent picture of the former Courthouse in Fabriano. (B) Historical photo before the raising (http://www.fabrianostorica.it/vecchiefoto/mestieri/lapesa.htm)

This constitutes the preliminary step in quantifying safety levels and supporting the design with proper strengthening interventions.

Historically, existing URM buildings were built by following the rule of thumb and not by standardized procedures. As a result, the modelling of URM structures is even more challenging due to all the uncertainties involved. In-situ tests allow for the acquisition of data on a local scale by providing details on the mechanical properties of materials, actual decay condition as well as structural information.[1] Unfortunately, these tests are often in short supply due to a lack of financial resources or conservation restrictions within the building. Moreover, other uncertainties, such as those related to the quality of wall-to-wall and wall-to-floor connections or the diaphragms' stiffness, are more effectively investigated by evaluating the issue directly on a global response scale. In this context, data from ambient vibration tests (AVTs) can be very useful to support seismic assessment procedures and to address the modelling choices.[2–4] In fact, they define a target for the numerical model's calibration thanks to the identification of the dynamic properties in terms of modal parameters. While literature reports several applications for reinforced-concrete (RC) or steel structures, especially bridges and other strategic infrastructures,[5,6] the examples on masonry buildings are very few. The latter are mostly addressed to monumental buildings,[7–10] especially towers and churches, and they usually adopt the finite element (FE) approach as a modelling strategy.[11–14] In addition, very few instrumented structures actually experienced an earthquake which allowed the model to be validated in the nonlinear field[15–17] and also towards different inputs.[18]

This paper illustrates the calibration and validation of a numerical model of the former Courthouse of Fabriano (Ancona, Marche) (Section 2). This is a strategic URM building selected as a case study in the ReLUIS project Task 4.1, funded by the Italian Department of Civil Protection (DPC) from 2017 to 2018. A permanent monitoring system was implemented in 2010 by the Italian Structural Seismic Monitoring Network (referred to as OSS in the following, i.e. through the Italian acronym of *Osservatorio Sismico delle Strutture*[19]). Moreover, it was struck by the Central Italy earthquake sequence in 2016/2017.[20] The equivalent frame (EF) model of the building has been developed by using the Tremuri software package.[21] The EF approach was advantageous due to its limited computational effort and efficiency to execute nonlinear static (NLSA) and dynamic (NDLA) analyses as well, which is useful for seismic assessment aims. The model has been firstly calibrated in the linear field (Section 4) through an iterative process, mainly based on the use of sensitivity analysis (Section 4.3). The target of the calibration process was the experimental modal parameters identified from some ambient noise (AN) recordings provided by OSS (Section 3). Then, the reliability of the EF model was validated also in the slight nonlinear range, by performing NLDA with some recordings acquired by the system during the 2016/2017 earthquake. In particular, the following entities have been adopted as targets for the validation (Section 5): the estimate of the activated inertial forces and the comparison in terms of accelerations and floor spectra on local sensors.

2 | CASE STUDY DESCRIPTION AND AVAILABLE DATA

2.1 | Geometrical data and structural details

The former Courthouse of Fabriano was originally built around 1940 (Figure 1A). Initially, it hosted the G.B. Milani Industrial School and later it became the seat of the court. Currently, a change of use is pending but it is expected to serve as a preservation site for strategic means. The structure is characterized by a T-shaped plan (average storey area equal to

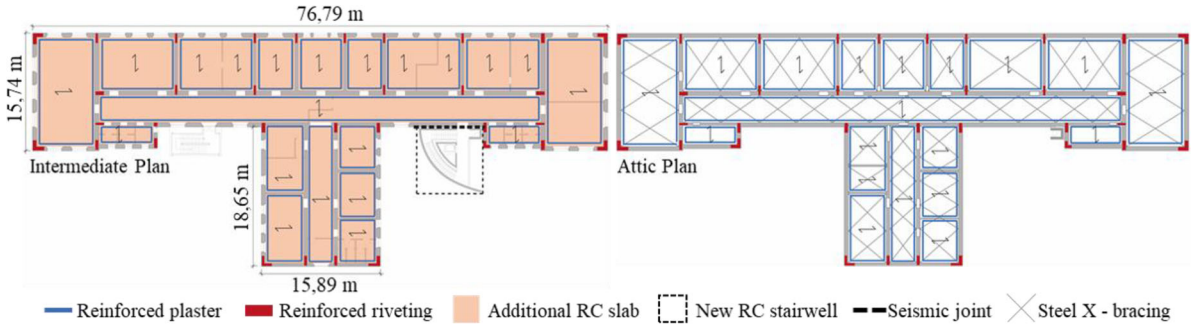

FIGURE 2 Main strengthening interventions realized in 1999 after the 1997 Umbria and Marche earthquake

1220 m^2, Figure 2) and is composed of three storeys and one basement (total height equal to 16.8 m). Originally, the building had only two storeys and a basement (Figure 1B); as a matter of fact, the last storey was raised in 1950.

The structure has regular masonry walls, horizontal slabs and a gabled trussed roof. In 1997, the Umbria and Marche earthquake damaged the building and exposed some structural weaknesses. Strengthening interventions were set in motion in 1999 to restore the damage caused and improve its seismic response. Figure 2 depicts the main structural interventions implemented viz. replacement of the original stairwell with a RC one, disconnected from the main building through a seismic joint; execution of local interventions on vertical walls (strengthened with reinforced plaster) and on horizontal floors (in some cases replaced, in others reinforced with an additional RC slab); strengthening of the roof by means of a steel X-bracing; the improvement of the wall-to-wall connections through reinforced riveting.

Thanks to the working drawings made available by OSS, a huge amount of data about the materials, geometry and structural details have been collected and used to set up the model. Moreover, all data were further verified by the authors during some in-situ inspections. These inspections were conducted within the research activities of Task 4.1 of the ReLUIS project.[20] The most important information to set up the numerical model is summarized in Figure 3.

In particular, Figure 3A illustrates the location of masonry typologies present in different stories of the building while Figure 3B depicts the vertical cross-sections. There are three main masonry typologies (M1, M2, and M3) that can be further classified depending on the realized strengthening interventions as follows:

- M1: Stone masonry (from 40 to 125 cm thick), widespread both in the internal and external walls of the basement, second floor and attic. The intervention with reinforced plaster (from 3.5 to 10 cm thick) was performed alternatively only on the internal side of the walls (M1_C1) or both sides (M1_C2).
- M2: Solid-brick masonry (from 25 to 65 cm thick), only present in the longitudinal internal wall of the last storey and some internal walls of the lower ones. The intervention with reinforced plaster (from 3.5 to 10 cm thick) was always performed on both sides of the wall.
- M3: Stone masonry with external brick face (from 50 to 90 cm thick), present in the perimeter walls of the first two levels. In this case, the intervention with reinforced plaster was performed only on the interior of the walls. Due to the significant thickness variation of the stone masonry leaf, in the analysis phase, M3 will be divided into two classes (M3_A and M3_B) to define equivalent mechanical parameters' values as described in further detail in Section 4.2.2.

Figure 3C in contrast shows the typologies of horizontal diaphragms:

- S1: slabs with H steel beams, small brick vaults and a 6 cm thick RC slab above added during the 1999 restoration. This stratigraphy is present in the diaphragms of the first two levels. An intervention through Φ16 bars guarantees the connection with the perimeter walls.
- S2: slabs with H steel beams, hollow clay blocks and an additional RC slab above. In this case, as well, the diaphragms were connected to the perimeter walls through Φ16 bars.
- S3: slabs with H steel beams, corrugated sheet and a 6 cm thick RC slab above. This typology was realized during the 1999 strengthening interventions to substitute the original horizontal floors. Since the in-situ inspections highlighted the presence of steel beams of two different dimensions (depending on the span), two subclasses were distinguished: S3_A (with IPE 240 beams) and S3_B (with IPE 160 beams). S3 slabs are connected with the masonry walls through a chemical anchorage.

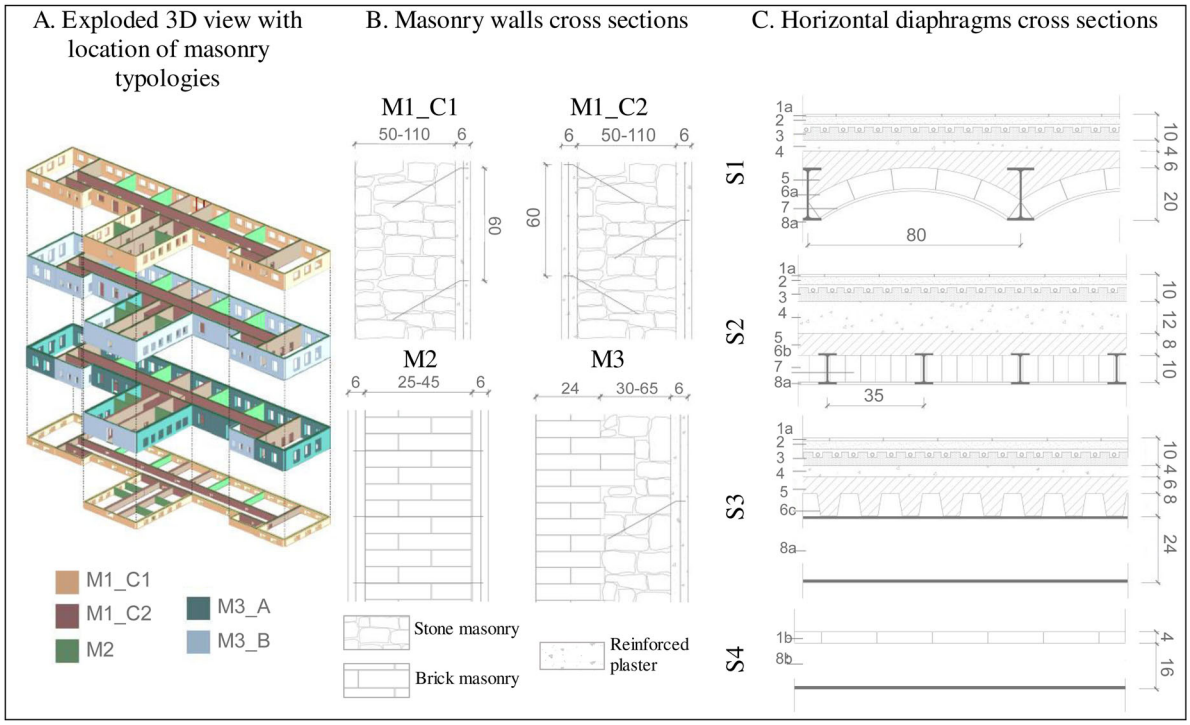

FIGURE 3 Exploded 3D view with location of masonry typologies (A), masonry walls cross-sections (B) and horizontal diaphragms cross-sections (C) in the building (units in cm). In (B), the thickness range of masonry leaves is indicated, too

- S4: in the attic exclusively. It is made of Ω-shape steel elements with on-centre spacing equal to 145 cm and wood flooring. Depending on the dimensions of the Ω -shape steel elements, S4 was distinguished in S4_A (if the steel element was 160 mm high) and S4_B (if it was smaller). For S4, the strengthening intervention was: (i) replacement of the old boarding; (ii) creation of Φ20 steel X-bracing; and (iii) improvement of the connection with the perimeter walls through steel bars injected with chemical anchorage.

In addition, the following data on soil type and the foundation system was available: the results of an MASW test performed close to the Courthouse, and the results of a video-endoscopy from which an embedment of foundation equal to 1.90 m was estimated. All these tests were performed by a company just before the OSS installed the accelerometers for the permanent monitoring of the structure. According to these data, the soil type was assumed to be B according to the classification criteria in Eurocode 8.[22]

2.2 | Data from the permanent monitoring system

As briefly introduced in Section 1, the former Courthouse of Fabriano was permanently instrumented by OSS by means of 28 accelerometers placed at different levels and one three-axial sensor located at the foundation (Figure 4A).

The dynamic monitoring system allows for the recording of acceleration time series at predefined intervals every day. It is also equipped with a trigger-based algorithm set to register the response if the acceleration values exceed some predefined thresholds (e.g., in case of a seismic event). Acceleration signals are acquired at a sampling frequency of 250 Hz and length of 3600 s (for the ambient vibrations noise) or 60 s (if the record exceeds the acceleration threshold).

Table 1 presents the recordings made available by the OSS for Task 4.1 Workgroup within the ReLUIS project.[20] The available data are distinguished among main shocks (E in the table), secondary events (SE), or AN. Furthermore, Table 1 provides synthetic data related to the date/time UTC and the peak ground acceleration (PGA) recorded in the two main

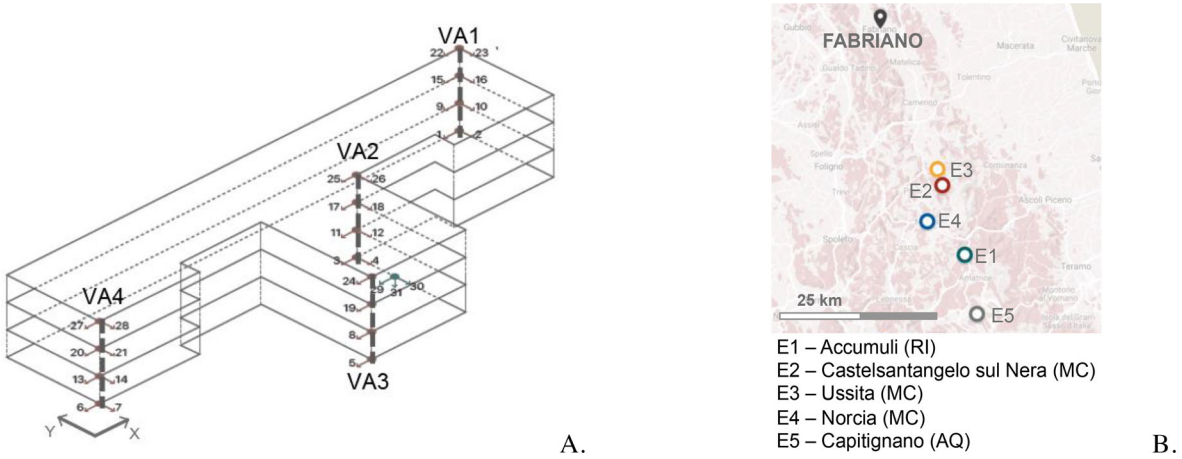

FIGURE 4 (A) Locations of the *Osservatorio Sismico delle Strutture* (OSS) sensors at the different stories (VA stands for Vertical Alignment). (B) Epicentres of the 2016/2017 earthquake sequence in Central Italy (main shocks)

TABLE 1 Available events for the model calibration and validation of the former Courthouse of Fabriano

Main shocks	Date and time (UTC)	PGA (g)		Other events	Date and time (UTC)	PGA (g)	
		X	Y			X	Y
E1	24/08/2016 01:36	0.042	0.054	SE1	08/10/2016 18:11	0.001	0.001
E2	26/10/2016 17:10	0.029	0.026	SE2	28/10/2016 13:56	0.001	0.001
E3	26/10/2016 19:18	0.082	0.088	SE3	03/11/2016 00:35	0.007	0.006
E4	30/10/2016 06:40	0.054	0.039	SE4	03/02/2017 05:40	0.001	0.001
E5	18/01/2017 10:14	0.008	0.007	AN	07/12/2016 15:14	–	–

Abbreviations: AN, ambient noise; E, event; PGA, peak ground acceleration; SE, secondary event; UTC, coordinated universal time.

directions of the building (as identified in Figure 4A). All main shocks refer to the 2016/2017 Central Italy earthquake sequence, whose epicentres are identified in Figure 4B. In particular, in the paper:

- the results of the dynamic identification (Section 3.1) performed using the ANs of December 7, 2016 (AN in Table 1) has been adopted as a target to calibrate the structural model in the elastic field (Section 4);
- the recording of the main shock of October 26, 2016 – 19:18 (E3 in Table 1) was adopted to perform the NLDA with the aim of validation (Section 5). In fact, shock E3 was the seismic event that hit the structure the most significantly due to its proximity to the building (Figure 4B);
- the other events have been used to corroborate further evidence on the dynamic characterization of the building (Section 3.2).

3 | DYNAMIC IDENTIFICATION

Time histories acquired under operational conditions (i.e., the AN of December 7, 2016) were processed using different output-only techniques both in the frequency and time domains. Thus, the modal identification was performed using only the 21 accelerometers installed at the second, third and fourth level of the building (from no. 8 to 28 in Figure 4A), excluding the triaxial sensor at the foundation (no. 29-30-31) and the sensors at the ground floor (from no. 1 to 7). The main aim was to extract modal parameters to verify the variability of results obtained and to corroborate the estimate of target values. The outcomes have been then adopted for the model calibration. Before analysing the signals, a high-pass filter with cut-off frequencies of 1 Hz was applied. The frequency domain modal analysis techniques include:

- the frequency domain decomposition (FDD)[23] and the enhanced frequency domain decomposition (EFDD),[24] both based on the singular value decomposition of the spectral density matrix of the acquired signal;

TABLE 2 Frequencies and modal assurance criterion (MAC) identified with different output-only techniques

	f (Hz)				MAC	
Mode	**EFDD**	**pLSCF**	**SSI-Cov**	**FDD**	**pLSCF – SSIcov**	**pLSCF –EFDD**
1	3.32	3.30	3.37	3.32	0.99	0.98
2	3.62	3.45	3.60	3.62	0.91	0.81
3	–	4.45	4.44	4.49	0.98	–
4	5.00	4.99	4.91	4.98	0.97	0.98
5	5.42	5.41	5.39	5.41	0.99	0.98
6	5.58	5.59	5.61	5.59	0.99	0.99
7	6.59	6.66	6.61	6.64	0.73	0.84
8	7.42	7.45	7.51	7.50	0.98	0.98

Abbreviations: EFDD, enhanced frequency domain decomposition; FDD, frequency domain decomposition; pLSCF, poly-reference least squares complex frequency; SSI-Cov, stochastic subspace identification covariance-driven.

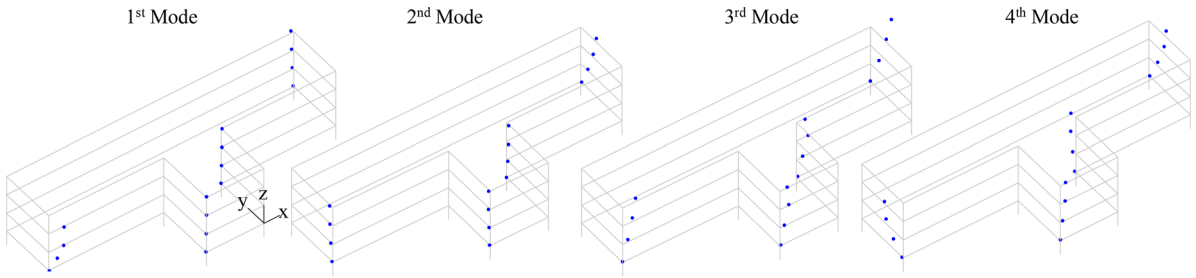

FIGURE 5 3D graphical representation of the modal displacements in the monitored points for the first four identified modes

- the poly-reference least squares complex frequency domain (pLSCF), a parametric technique to reduce the dependency of identification results on the user's choices (thanks to the stabilization diagram[25]).

Regarding the time-domain techniques, the stochastic subspace identification covariance-driven (SSI-Cov)[26,27] has been used. Through the combined use of the aforementioned output-only techniques, the first 8 modes of the building were identified, as discussed in more detail in Section 3.1.

Finally, the recordings acquired after the seismic events were processed with input–output techniques. Achieved by the use of the parametric method in the time domain called combined deterministic stochastic subspace identification (CSI).[28]

3.1 | Dynamic identification under operational conditions (output-only techniques)

Table 2 presents the natural frequencies obtained by the various techniques introduced in Section 3. Furthermore, it summarizes the modal assurance criterion (MAC) index[29] calculated alternatively between the couples of eigenvectors obtained through the aforementioned algorithms (namely pLSCF, EFDD, and SSI-Cov). As can be observed, the values of the identified frequencies are all very close to each other, also for the higher modes. Moreover, the MAC index highlights the excellent correlation between the mode shapes (with values higher than 90%). This correlation was confirmed through the application of various techniques.

Figure 5 presents a 3D graphical representation of the eigenvectors' components of the first four identified modes. The blue dots indicate the modal displacements of the monitored points. This schematic 3D view was created to avoid the introduction of any hypotheses on the relationship between the points of the structure, at least at this stage. In particular: the first ($f = 3.30$ Hz) and second ($f = 3.45$ Hz) modes activate the transversal response of the two wings in the Y direction; the third mode ($f = 4.45$ Hz) is in the X direction, while the fourth mode ($f = 4.99$ Hz) is torsional.

TABLE 3 Frequencies (Hz) during the seismic events

Mode	Event ID									
	E1	**SE1**	**E2**	**E3**	**SE2**	**E4**	**SE3**	**AN**	**E5**	**SE4**
1	3.20	–	3.30	2.36	–	2.40	–	**3.37**	2.81	3.16
2	–	3.91	–	–	3.46	2.81	3.17	**3.60**	3.23	3.52
3	4.31	4.78	4.24	3.91	4.34	3.48	4.29	**4.44**	4.26	4.50
4	4.63	5.33	4.82	4.05	4.82	3.99	4.58	**4.91**	4.90	5.06
5	–	5.53	–	–	–	4.37	4.88	**5.39**	5.09	5.42
6	5.12	5.94	–	–	5.37	–	5.00	**5.61**	–	5.52
7	5.82	6.83	–	–	–	–	–	**6.61**	5.93	6.87
8	6.63	–	6.79	–	6.89	5.74	6.26	**7.51**	6.51	–

Abbreviations: AN, ambient noise; E, event; SE, secondary event.

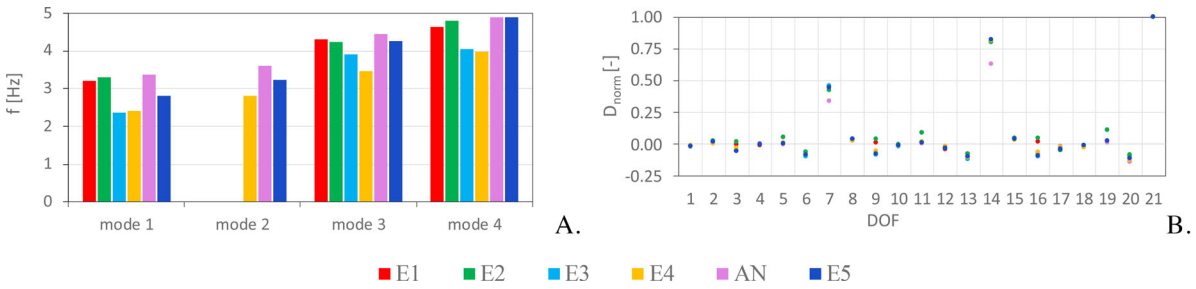

FIGURE 6 (A) Natural frequency wandering of the first four modes obtained by data analysis from main shocks and ambient vibrations. (B) Normalized modal displacements of mode 1 for each degree of freedom (DOF) of the structure for the same recordings

3.2 | Analysis of the dynamic response during the seismic events (input–output analysis)

Modal parameters were also identified using the time histories recorded during the main shocks and aftershocks. In this case, the input–output CSI technique was adopted. The input is represented by the signals measured from the three-axial sensor at the base of the structure. Outputs, however, are the response of the building which were recorded by sensors installed at the different storeys (Figure 4A). Table 3 summarizes the natural frequencies identified from the accessible recordings, i.e. the five main shocks (E) and the four aftershocks (SE) listed in Table 1 plus the AN recording, highlighted in bold. The identified frequencies present a noticeable variation across the entire set of observed seismic events (Figure 6A). Moreover, it is possible to observe an irregular change in these frequencies when their layout is chronological. The maximum frequency values (for all the vibration modes) can be observed from the analysis of the AN, even if this record was acquired after the most significant seismic events of the earthquake swarm.

An additional representation of the amplitude variation of modal parameters on seismic events is presented in Figure 7, in which natural frequencies are plotted in function of three earthquake severity indexes. They consist of (A) PGA, the maximum peak ground acceleration recorded at the building base; (B) PSA, the maximum (over all the channels) absolute value of the peak structural acceleration recorded on the structure; and (C) the maximum recorded- drift, derived from the displacement time histories at various levels of the structures obtained through a double integration of acceleration signals. An inverse linear correlation between the modal frequencies and the adopted indexes was found for the first four modes.

This "wandering" of fundamental frequencies of vibration in buildings is a known phenomenon in literature.[30–32] This is observed in the presence but also the absence of structural damage.[30] In particular, such a variation is an amplitude-dependent phenomenon, that can be composed of a transient – reversible- contribution and a permanent -irreversible – contribution. As already highlighted by Ceravolo et al.[30] and Lorenzoni et al.,[33] the reversible phenomenon is mainly ascribable to: reversible material (e.g., temporary micro-cracking and sliding effects) and geometrical nonlinearities; soil-structure interaction (SSI); interaction between structural and non-structural elements. If no structural damage occurs, the frequency shift gradually vanishes with time and the pre-seismic values of fundamental frequencies are completely recovered.

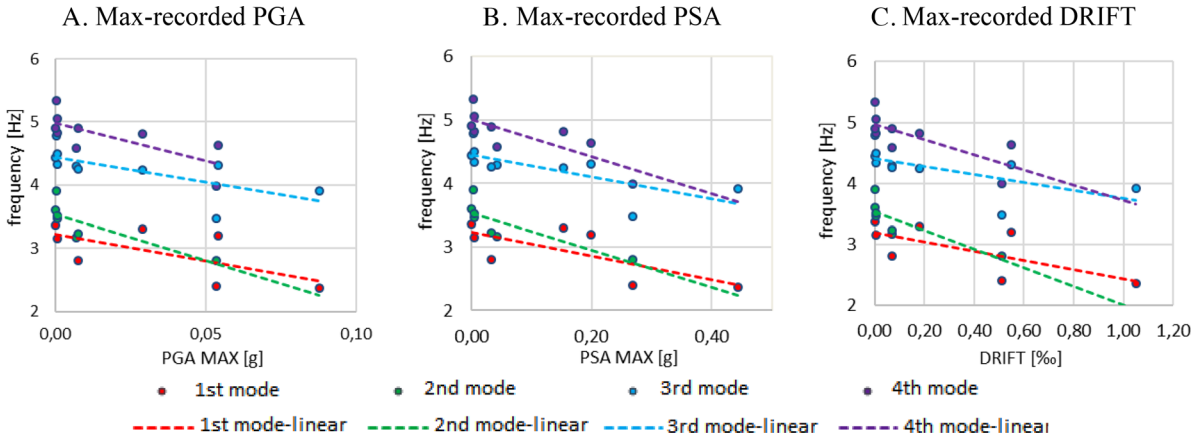

FIGURE 7 Seismic wandering of the modal frequencies as a function of (A) peak ground acceleration (PGA), (B) peak structural acceleration (PSA), and (C) drift during the main shocks of the earthquake swarm. A linear fitting of data is assumed

In the specific case of the former Courthouse of Fabriano, the in-situ surveys carried out did not detect any significant structural damage (none that would produce any noticeable variations in dynamic behaviour). Nonetheless, it did suggest that the "wandering" of the modal properties can be mainly attributed to the reversible nonlinear phenomena of the overall system with respect to the shaking level rather than a global stiffness decay of the structure caused by damage.

In order to confirm this hypothesis, the variation of normalized modal displacements (D_{norm}) at different locations was analysed. This variation is illustrated in Figure 6B, by way of example for the first mode but analogous results have been obtained for the other modes, as well. In particular, the figure shows that: in the X-axis, the degrees of freedom (DOF) of the structure are associated with the points where accelerometers were installed (see Figure 4A); in the Y-axis, the normalized modal displacement is assessed using the dynamic identification values (normalized to the maximum displacement component). The displacements are illustrated to represent the different available recordings in order to highlight possible variation from one event to the next (due to seismic damage or degradation effects). It is possible to observe that, for each DOF of the structure, the corresponding modal displacement remains almost unchanged, meaning that no significant variation of the corresponding mode shapes occurred (e.g., ascribable to stiffness degradation of diaphragms).

4 | MODEL CALIBRATION IN THE ELASTIC FIELD

4.1 | Criteria adopted for the calibration

Thanks to the detailed data on the geometry, structural details and materials (Section 2.1), it was possible to set up a preliminary structural model. However, despite the accuracy of the available data, the modelling process is still influenced by both aleatory (i) and epistemic (ii) uncertainties:

(i) Aleatory uncertainties associated with mechanical properties of materials. They are hereinafter identified as X_{i} (with $i = 1 \ldots N$), where X_{i} can alternatively collect either a single variable or a set of fully correlated variables. The aleatory uncertainties are treated as random variables by defining a plausible range of variation ($X_{\text{i, low}} - X_{\text{i, up}}$).
(ii) Epistemic uncertainties associated with the effectiveness of structural details. Since, in most cases, the latter can barely be quantified through continuous variables, they are dealt with by taking into consideration alternative structural models. They are hereinafter identified as $Y_{\text{j, m}}$ (with $j = 1 \ldots M$ and where m are the alternative considered models).

To address the model calibration process while dealing with the uncertainties, a variety of model updating methods could be used,[34–36] for example, direct (non-iterative) techniques (direct matrix updating or method and error matrix) or iterative techniques (eigen-dynamic constraint, inverse eigen-sensitivity or response function methods). The first ones directly update the stiffness and mass matrices, computing a closed-form solution through the structural equations of motion and taking advantage of the orthogonality properties of modes. These techniques are computationally very efficient but can bring to parameters that are not always physically meaningful.

Conversely, in the examined case, the model calibration was performed by implementing an iterative technique based on the use of sensitivity analysis. This estimates the effects caused by the different uncertainties and identifies those which affect the global response the most. The target for the model calibration in the elastic field is the results of the dynamic identification carried out with the AN of December 7, 2016, and with the SSI-Cov algorithm (Table 2). Although this method can be computationally less efficient, the results are generally more consistent on a physical basis.

In particular, the calibration procedure used consists of three consecutive steps:

1. The execution of simplified sensitivity analysis for the epistemic variables, to identify the most reliable modelling choice, and for the aleatory variables, to understand those affecting the elastic response most. The results of this preliminary sensitivity analysis identify the variables to be taken into account in step 2, with little computational effort and the possibility to directly verify the consistency between numerical results and physical meaning from an engineering perspective. More specifically, when it comes to the aleatory uncertainties, the "star design with a central point approach" has been adopted.[37] This approach limits the numerical analyses to be performed to $2N + 1$ (where N is the number of uncertain variables or group of variables). Each one of the $2N$ models is obtained by considering the median values of all the uncertainties except for one (namely the investigated aleatory variable). It is set once at the lower value of the range ($X_{i,\,low}$) and once at the upper one ($X_{i,\,up}$). The additional analysis ("+1") is instead performed by setting all the parameters to their median values. For the epistemic uncertainties, alternative models were considered, where all the mechanical parameters were set to their median values (as in the "+1" analysis).
2. The execution of a complete factorial analysis on the sub-set of aleatory variables set in step 1. It aims to understand the setting of variables (e.g., increasing or decreasing their value) and to identify their most efficient combination (e.g., increasing some variables, while decreasing others). In this step, $2^{N'}$ analyses were performed, where N' ($<N$) are the only aleatory variables found to be significant in step 1.
3. The final optimization of the model calibration. In this last step, the parameters identified in step 1 were modified according to the rules defined in step 2. This was done in order to obtain the best fit between the numerical model and the experimental data, that is, minimizing the error with respect to the target solution.

In the following section, the basic assumptions made to set the model are discussed, including the list of examined uncertainties (Sections 4.2.2 and 4.2.3). The results of the three aforementioned steps are illustrated in Section 4.3.

4.2 | Setting of the numerical model

4.2.1 | Modelling approach and variables assumed as deterministic

The structural model was set up with the 3Muri software.[38] The software is based on the EF modelling approach, which considers only the in-plane behaviour of masonry walls and concentrates the deformability and the nonlinear behaviour into specific portions of URM walls, namely piers (vertical elements) and spandrels (masonry beams that connect piers). This approach is assumed to be reliable when the box behaviour is guaranteed. In the examined case, the data acquired on structural details, the results of the dynamic identification and the analysis of the damage that occurred after the 2016/2017 earthquake unanimously highlight that it is possible to assume a global behaviour.

The first step in EF modelling is the idealization of URM walls into equivalent frames (Figure 8A–B). Therefore, each wall is discretized by a set of masonry panels modelled as beams (piers and spandrels), connected by rigid areas (nodes). In Figure 8B, the dashed lines connect the barycentre of the structural element with the nodes to which it is linked.

This step affects not only the nonlinear phase of the response (by assuming a priori the regions where cracks and nonlinearity will develop), but it also influences the elastic field. The definition of rigid areas can also potentially alter the actual deformability of the walls. Although different criteria have been proposed in the literature for the mesh geometry definition,[21,39–41] no shared rules have yet been unanimously outlined. Recent research[42] parametrically analysed the sensitivity due to these criteria and compared the results of detailed FE and EF models. It highlighted that, in general, the dispersion of the results considerably increases with a pronounced irregularity in the opening patterns, especially in the nonlinear field. Moreover, both Cattari et al.[42] and Ottonelli et al.[43] recognized that the criteria proposed in Lagomarsino et al.[21] and Dolce[40] give reliable results. For these reasons, in the examined case, the dimensions of piers and spandrels have been considered as a deterministic variable, defined according to the criteria proposed in Lagomarsino et al.[21] Hence, it has verified that the resulting rigid areas were not too big to limit the alterations induced in the walls' stiffness (Figure 8B).

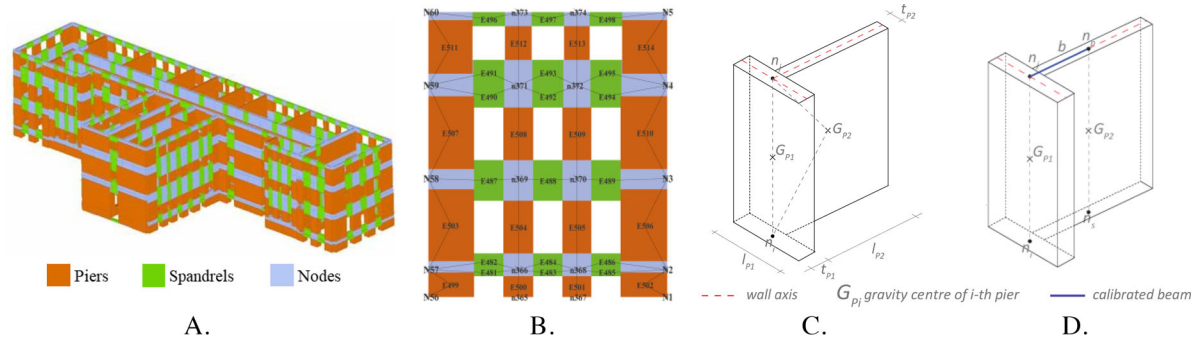

FIGURE 8 Structural 3D model of (A) the former Courthouse in Fabriano and (B) mesh of one wall. Modelling strategies for the flange effect: (C) full kinematic coupling or (D) intermediate coupling through calibrated beams

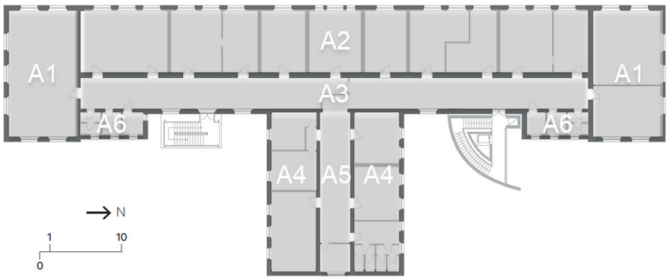

	Level 1	Level 2	Level 3	Level 4
A1	90-10%	90-10%	90-10%	90-10%
A2	95-5%	95-5%	95-5%	95-5%
A3	100%	100%	100%	100%
A4	90-10%	90-10%	90-10%	90-10%
A5	90-10%	90-10%	95-5%	95-5%
A6	90-10%	90-10%	90-10%	90-10%

FIGURE 9 Load percentage assumed for diaphragms at the different levels (the first percentage refers to the main orientation, the second one to the orthogonal direction)

Once defined, the 2D modelling of the walls was used to construct the whole 3D model by introducing the diaphragms. The latter are modelled in 3Muri as 3- or 4-nodes finite orthotropic membrane elements,[21] identified by the Young modulus E_{1eq} along the principal direction (floor spanning orientation), the Young modulus along the perpendicular direction E_{2eq}, the Poisson ratio ν and the shear modulus G_{eq}.

In the examined case study, the uncertainty associated with the diaphragm load was treated as a deterministic variable, since an accurate stratigraphy was available for all the diaphragms (Figure 3C). The diaphragm mass is not dominant (about 30%), since masonry walls are massive. Concerning the stiffness properties, E_{1eq} and E_{2eq} were considered deterministic and set to a value ranging from 5122 to 18690 MPa, as a function of the diaphragm typology. Conversely, only G_{eq} has been considered as an epistemic uncertainty, being the most significant parameter in influencing the tangential stiffness, coupling walls and redistributing seismic forces (both in linear and nonlinear phases).

The loads are transferred to vertical walls according to the floor spanning orientation identified in Figure 2. It was assumed that a small load percentage is also supported by the orthogonal walls, considering that the diaphragms were strengthened with a RC slab. This percentage was set between 5 and 10% (depending on the floor typologies) and treated as a deterministic variable (Figure 9). Indeed, preliminary analyses highlighted that the effects of different load percentages on the modal response are irrelevant and insignificant in the nonlinear field, where different mass repartition modifies the stress on the piers and, consequently, their strength.

Finally, the model was considered as fixed at the base. Some preliminary analyses were carried out to investigate the possible effect of the SSI on the structural response, as this could be significant even in the elastic field.[18,44] To this aim, a shear modulus equal to 194 MPa was first assumed for the soil in the elastic condition. A compliant base model in which equivalent linear springs – calibrated according to Gazetas[45] – were placed under each pier at the base of the EF model was then made. The dynamic identification carried out on this model suggested a possible elongation of the period (around 15%) due to the SSI interaction, which was confirmed by also adopting the more simplified replacement oscillator approach proposed in Maravas et al.[46] It was also verified that the change in the mode shapes produced by the SSI was negligible.

These results substantially confirm that this uncertainty is less significant than the others examined in this paper and justifies neglecting it. This assumption is further corroborated by the fact that the soil properties around the building are

TABLE 4 Range of variation of the aleatory uncertainties assumed in step 1 of the calibration process and values adopted in the final model (step 3)

		Step 1 of the calibration phase						Final values adopted after the calibration	
		E (N/mm^2)		G (N/mm^2)					
X_i ($i = 1\ldots16$)		$X_{i,low}$	$X_{i,up}$	$X_{i,low}$	$X_{i,up}$	k_1 (–)	k_2 (–)	E (N/mm^2)	G (N/mm^2)
Piers	$X_1 = X_{11}$ = M1_C1	1500	3089	500	1030	1.2	1.3	3089	1030
	$X_2 = X_{13}$ = M1_C2	1500	3861	500	1287	1.5	1.3	3089	1030
	$X_3 = X_{12}$ = M2	1200	4050	400	1350	1.5	1.5	4050	1350
	X_4 = M3_A	1412	3006	471	1002	1.2	1.3	1412	471
	X_5 = M3_B	1372	2969	457	990	1.2	1.3	2969	990
Spandrels	$X_6 = X_{16}$ = M1_F	1500	2574	500	858	–	1.3	2574	858
	$X_7 = X_{14}$ = M1_C1_F	1500	3089	500	1030	1.2	1.3	3089	1030
	$X_8 = X_{15}$ = M1_C2_F	1500	3861	500	1287	1.5	1.3	3089	1030
	X_9 = M2_F	1200	4050	400	1350	1.5	1.5	4050	1350
	X_{10} = M3_F	1200	2700	400	900	–	1.5	2700	900

not particularly poor. In addition, the analysis of the H/V spectral ratio values provided by the MASW test did not suggest any resonance frequency caused by the soil properties.

4.2.2 | Definition of the uncertainties described through continuous variables

According to Section 4.1, 16 aleatory variables X_i ($i = 1\ldots16$), associated with the masonry mechanical properties (Young Modulus E and Shear Modulus G) were considered. The values are differentiated for each masonry typology (Figure 3A–B), and piers and spandrels. The masonry of the last storey raised in 1950 has been considered as an independent variable, as well. Table 4 summarizes the range of variation of E and G assumed for piers and spandrels in step 1 of the sensitivity analysis, and the values assumed in the final calibration of the numerical model, at the end of step 3. In Table 4, the variables from 11 to 16 refer to the raised level; the ID assigned to each masonry typology corresponds to that introduced in Section 2.1.

The range of variation of E and G has been defined according to the reference values proposed in the Commentary of the Italian Technical Code,[47] as well as the values of corrective coefficients (k_1 and k_2 in Table 4) that account for the presence of constructive details, such as strengthening interventions or good quality mortar, etc. The values have been also confirmed by some experimental tests available in the literature.[1,48]

Concerning the piers:

- For stone masonry (M1) and solid bricks masonry (M2): the minimum value ($X_{i,low}$) corresponds to the minimum one proposed in the Commentary of the Italian Technical Code[47] for the corresponding masonry typology, while the maximum value ($X_{i,up}$) corresponds to the maximum one proposed in the Commentary of the Italian Technical Code[47] multiplied by k_1, to take into account the intervention with reinforced plaster of 1999, and k_2, to consider the presence of good quality mortar. Concerning k_1, the value of 1.5 was assumed for the walls strengthened on both sides (in agreement with the above mentioned Commentary[47]), while the value of 1.2 for those strengthened only on one side.
- For M3 (stone masonry with an external brick face, masonry type not covered by the Commentary of the Italian Technical Code[47]), the elastic modulus was estimated as a weighted mean accounting for the two masonry types and their actual thickness. As a result, two classes were considered depending on the actual thickness: M3_A (thickness range: 78–90 cm) and M3_B (thickness range: 50–65 cm).

Concerning the spandrels:

- For those characterized by the same thickness of the adjacent piers, the same mechanical properties of the corresponding pier were considered (M1_C1_F, M1_C2_F and M2_F).
- For those placed in the perimeter walls, which were strengthened with reinforced-plaster only on the interior of the wall, the assumed parameters are those of the corresponding pier without the application of corrective coefficient k_1 (M1_F and M3_F, this latter assumed to have been built with bricks).

TABLE 5 Thickness and stiffness properties assumed for orthotropic membranes

Set of parameters	Membrane	t_{eq} (cm)	G_{eq} (N/mm^2)
Set A	S1	6.0	12540
	S2		
	S3	9.0	13125
Set B	S4	3.5	700

4.2.3 | Definition of the uncertainties described through alternative models

According to Section 4.1, four epistemic variables $Y_{j,m}$ ($j = 1 \ldots 4$) were considered, including Y_1 = Flange effect, Y_2 = role of the basement, Y_3 = effectiveness of the seismic joint between the RC staircase body and the building, and Y_4 = horizontal diaphragms' stiffness.

Regarding the *flange effect* (Y_1 in Table 6), the sensitivity analyses were mainly aimed at investigating the effects connected to the actual length of the orthogonal pier where stress redistribution is possible.

In general, different solutions can be implemented in the software packages to model the coupling between orthogonal walls. 3Muri (Figure 8C) adopts by default a perfect coupling, by defining 3D nodes that provide a full kinematic coupling of the vertical displacement component in orthogonal walls. This is computationally effective, but it may lead to an overestimation of the flange effect in presence of flanges with significant width, as it takes the full width into account. Despite this, it is possible to introduce a proper equivalent beam (Figure 8D) with stiffness calibrated to account for the actual stiffness of the interacting piers. To this aim, the default equivalent idealization provided by 3Muri (Figure 8C) has been modified by introducing some extra nodes (n_s and n_p in Figure 8D) and a beam element (b marked in blue in Figure 8D) connecting the two orthogonal piers.

Thus, the following cases were investigated as alternative options: (a) full kinematic coupling; (b) calibrated equivalent beam; (c) effect of a poor wall-to-wall connection simulated by an equivalent beam of negligible stiffness. In case (b), the beam stiffness has been computed on the basis of the piers geometry (t_{Pi} and l_{Pi} in Figure 8C) by considering only the contribution of the length expected to be involved in the stress redistribution (i.e., by eventually considering a length l_{Pi} lower than the actual one, computed according to Eurocode 6[49]).

Indeed, the third case (c) is not representative of the former Courthouse of Fabriano, as the quality of the wall-to-wall connection was guaranteed by previous retrofitting interventions (as described in Section 2.1), but it was analysed anyway to investigate this effect which can be relevant to existing URM buildings.

As far as the *role of the basement* is concerned (Y_2 in Table 6), two alternative models were studied: (a) only the above-ground part (1.55 m height) has been modelled; (b) all the height of the basement has been modelled (3.66 m height), assuming negligible restrain effects from the ground.

The *effectiveness of the seismic joint* (Y_3 in Table 6) is associated with the connection between the main body of the building and the RC stairwell and was modelled through equivalent orthotropic membranes. Three alternative cases were considered: (a) full effective seismic joint, in which the staircase body was not modelled; (b) not effective seismic joint, in which the orthotropic membranes are considered infinitely stiff; (c) intermediate condition, with a finite value of stiffness for the orthotropic membranes.

As far as the *diaphragms shear stiffness* concerns (Y_4 in Table 6), only the modulus G_{eq} has been considered as an epistemic uncertainty. The value of G_{eq} allows accounting for two contributions: the actual floors stiffness and the effectiveness of the wall-to-floor connection. Table 5 collects the values of thickness t_{eq} and the shear stiffness G_{eq} assigned to the orthotropic membranes. The values refer to the following assumptions: diaphragms are well connected to walls, and representative of actual homogenized values of the materials that characterize the stratigraphy of the diaphragms (option a in Table 6). In particular, Set A collects the diaphragms of the first three levels (S1, S2 and S3 in Section 2.1) retrofitted with a RC slab, while Set B refers to the timber floors of the upper level (S4), retrofitted with steel X-bracing, and the roof. Starting from option a, three additional cases were considered, characterized by G_{eq} values representative of (b) infinitely rigid diaphragms; (c) flexible diaphragms; and (d) different stiffening roles of the various wings of the T-shaped plan. Options (b) and (c) were simulated to increase or decrease, respectively, by two orders of magnitude the G_{eq} values (see Table 5). In contrast, option (d) includes two alternatives: (d1) stiffening the diaphragms of areas A4/A5 (see Figure 9, named as part "T"), while the others were set to the values of Table 5; (d2) stiffening the diaphragms of areas

TABLE 6 Considered epistemic uncertainties (in bold the ones assumed in the validation phase)

	Option (*m*)			
Y_j	**a**	**b**	**c**	**d**
Y_1 = flange effect	Full kinematic coupling	**Calibrated equivalent beam**	Poor wall-to-wall connection quality	
Y_2 = role of basement	**Restrain effect of the ground considered**	Restrain effect of the ground neglected		
Y_3 = effectiveness of the seismic joint	**Seismic joint fully effective**	Seismic joint ineffective	Intermediate condition	
Y_4 = diaphragm stiffness	Actual values	Infinitely rigid	Flexible	**Values differentiated for T and R parts**

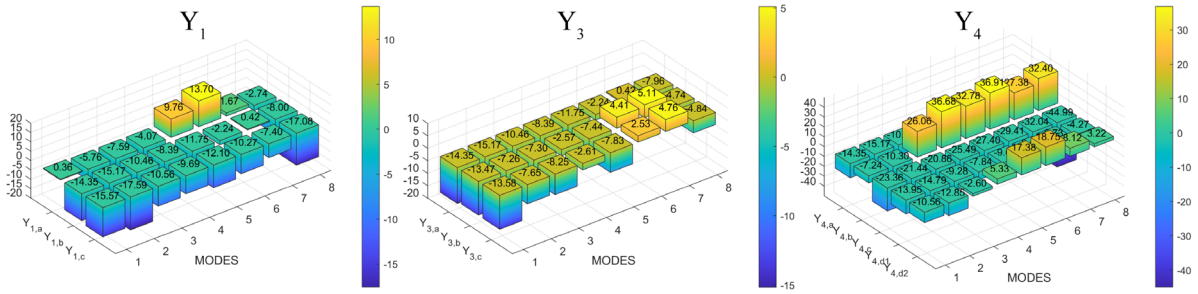

FIGURE 10 Results in terms of error per cent (err%)

A1/A2/A3/A6 (see Figure 9, named as part “R”). This further study is justified by the fact that portions of the floors of part "T" are smaller than those of part "R"; thus, the stiffening effect could be bigger. In this case, the stiffening was simulated by increasing the values listed in Table 5 by only one order of magnitude.

Table 6 summarizes all the considered epistemic uncertainties $Y_{j,m}$. The most reliable results obtained from step 1 of the sensitivity analysis are highlighted in bold (as discussed more in detail in Section 4.3). The latter are those assumed in steps 2 and 3 and, finally, in the validation phase.

4.3 | Results of sensitivity analysis

This Section presents the results of the sensitivity analysis performed following the three steps described in Section 4.1. Numerical results were compared to the target ones assessing the percentage error (err%) on the natural periods and calculating the MAC index[29] between experimental and numerical mode shapes. The effects on the dynamic response of the epistemic uncertainties are presented separately (step 1, Section 4.3.1) and so are the influences of the aleatory variables (steps 1, 2, and 3, Section 4.3.2).

4.3.1 | Influence of uncertainties described through alternative models

Figures 10 and 11 show the err% on the first eight natural periods and the MAC index for the four modal shapes respectively. A variation of models was considered for each epistemic variable. The results refer to models set at the mean values of the parameters treated as aleatory uncertainties and defined in step 1 (see Table 4).

Concerning the flange effect (Y_1), it is interesting to note that option (a) (full kinematic coupling) produce the lowest error in terms of the period (Figure 10), but also the highest discrepancy in terms of mode shapes (Figure 11). Taking into account a more realistic coupling among walls through the calibration of the equivalent beam produces the right inversion of the first two modes. This results in a better agreement in terms of MAC; for this reason, option (b) has been considered to be the most reliable, also because moving from option (b) to (c), the results steadily get worse due to the

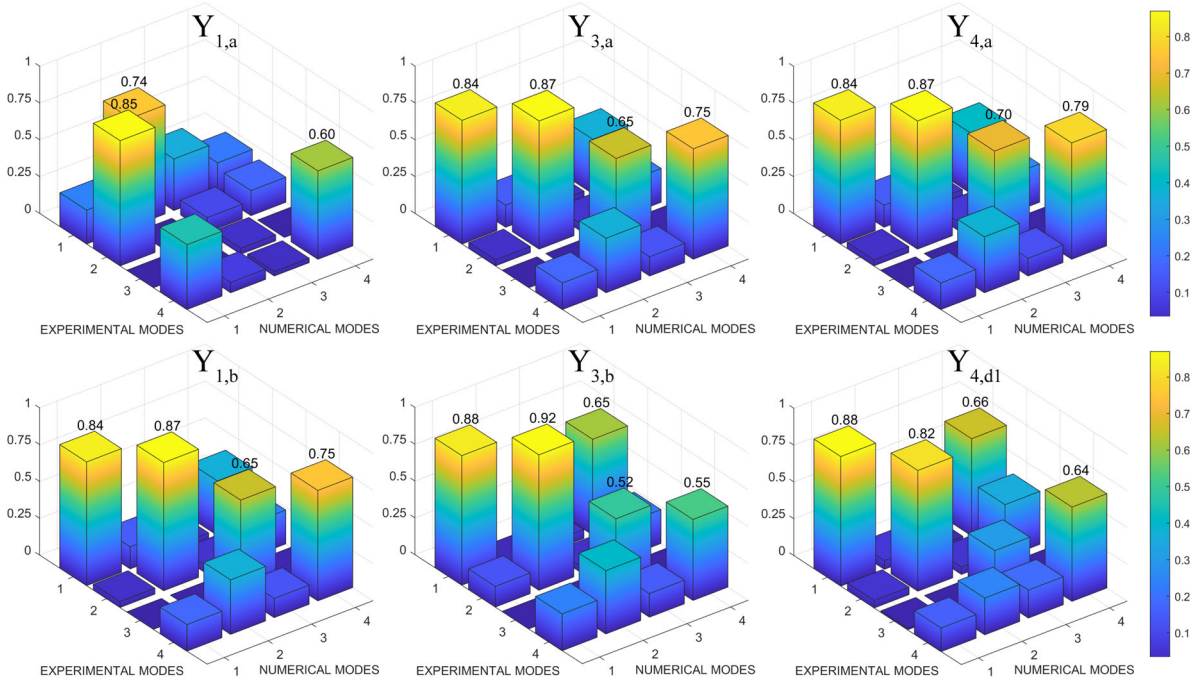

FIGURE 11 Results in terms of modal assurance criterion (MAC) index

fact that the wall-to-wall connection is rather good in this structure. Concerning the height of the basement floor (Y_2), the results of the sensitivity analysis demonstrated that this uncertainty does not noticeably affect the mode shapes. As expected, modelling the whole height of the basement determines a more flexible model, with percentage error on the fundamental period equal to –14.35% for $Y_{2,a}$ and –21% for $Y_{2,b}$, respectively. The strategy assumed as the most reliable is the one in which only the part of the basement placed above-ground is modelled ($Y_{2,a}$ in Table 6).

Concerning the role of the seismic joint (Y_3), the results of the sensitivity analysis reported that, when considered effective ($Y_{3,a}$ in Figure 11), higher values of the MAC matrix on the diagonal are observed as well as the stabilization of the global response. Despite that, the uncertainty of this variable does not significantly affect the results in terms of err% on the periods (Figure 10). During further analyses, the seismic joint was considered fully effective.

Finally, the results of the sensitivity analysis based on diaphragm stiffness (Y_4) showed that infinite stiff membranes ($Y_{4,b}$) or flexible membranes ($Y_{4,c}$) resulted in an unfavourable correlation between the experimental target in terms of mode shape. Indeed, although the MAC values of the first two modes are quite high, the MAC matrixes are not completely diagonal. Focusing on the effects of stiffening, when stiffening only part "R" ($Y_{4,d2}$), the MAC matrix is not diagonal, similarly to what occurs in the case of option $Y_{4,b}$. For this reason, Figure 11 presents the MAC values obtained by using option $Y_{4,d1}$. In the analyses presented hereinafter, the Y_4 variable is adopted by assuming the values of parameters summarized in Table 5, and by increasing the stiffness of the "T" part only.

4.3.2 | Influence of uncertainties described through continuous variables and calibration optimization

Concerning step 1 of the sensitivity analysis, Figure 12 illustrates the sensitivity factors S_n calculated as:

$$S_n = \frac{R_{max} - R_{min}}{0.5\,(R_{max} + R_{min})} \cdot \frac{0.5\,(P_{max} + P_{min})}{P_{max} - P_{min}} \tag{1}$$

where:

- R_{max} and R_{min} are, respectively, the maximum and minimum response of the model in terms of frequency.
- P_{max} and P_{min} are, respectively, the maximum and minimum values adopted for the parameter.

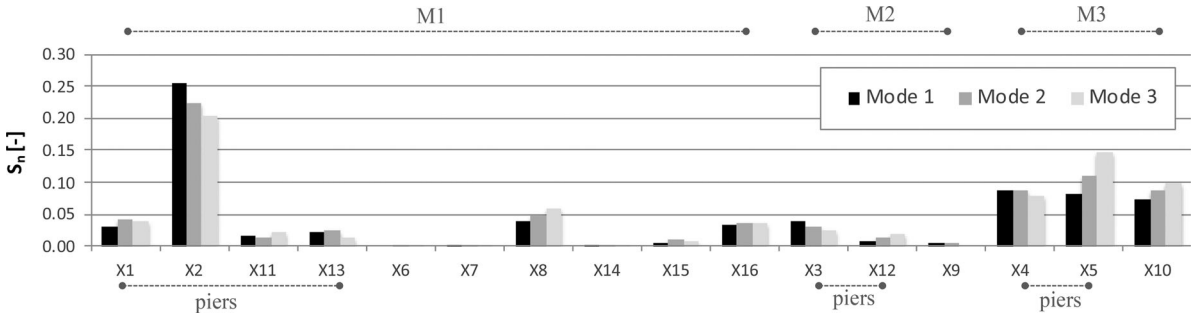

FIGURE 12 Sensitivity factors to aleatory variables

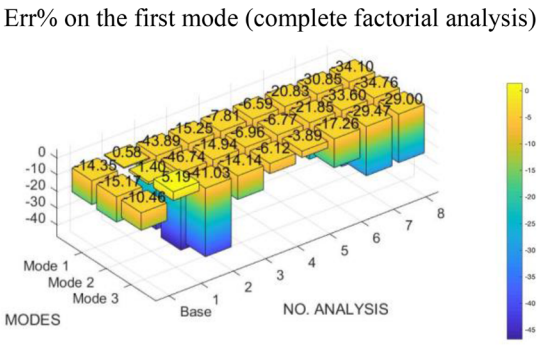

Legend			
No. Analysis	[a] M1	[b] M2	[c] M3
1	max	max	max
2	min	min	min
3	max	min	min
4	max	max	min
5	max	min	max
6	min	max	max
7	min	max	min
8	min	min	max

[a] M1 includes M1_C1, M1_C2, M1_F, M1_C1_F, M1_C2_F; [b] M2 includes M2, M2_F; [c] M3 includes M3_A, M3_B, M3_F

FIGURE 13 Errors per cent obtained from factorial analysis (step 2 of sensitivity analysis)

Results highlight that the dynamic response is more sensitive to the differences among the three predominant masonry types (M1-stone masonry, M2-brick masonry and M3-stone masonry with external brick face) rather than the differences individuated within each sub-category. Moreover, as expected, the role of piers was dominant with respect to that of spandrels.

Hence, in step 2, all the masonry typologies first defined were grouped into three groups of variables (M1, M2, and M3), in which all the sub-categories were characterized by the same materials used. The latter was treated as correlated variables, thus in the factorial analysis (step 2), they were varied between their respective minimum or maximum values simultaneously. Figure 13 presents the results of the complete factorial analysis on the first three modes in terms of err% with respect to the experimental target. From these results, it is possible to observe that better results are generally obtained by setting the mechanical parameters to the maximum value of the range for all the masonry typologies. However, to obtain the best fitting in terms of modal shapes it is necessary to decrease some parameters.

Finally, passing to step 3, the numerical model was optimized by varying the values of parameters on basis of evidence from step 2 to guarantee the best fit in terms of both natural periods and modal shapes. The comparison between the calibrated model and the experimental target are summarized in Figure 14 that presents for the final model: the percentage of participant mass and periods (Figure 14A); the err% of the periods compared to the experimental target (Figure 14B); the MAC index (Figure 14C). The mechanical parameters assumed in step 3 are summarized in Table 4. Finally, Figure 15 shows the mode shapes of the calibrated model; due to the high values of the MAC index, they also provide an in-plan overview and a more comprehensive reconstruction of the experimental modes depicted in Figure 5.

It is interesting to point out that the correlation between modes two and four (which one can see in Figure 14C) has also been highlighted in the AutoMAC calculated on the basis of experimental results, underlining a further coherence with the numerical model. From Figure 14 it is possible to see that err% and MAC on the first four modes, which are the ones that activated the most significant participant mass (close to 70%) are quite good. Moreover, it was verified that the higher modes are local modes and that they do not activate significant participant masses.

A.

Participant Mass

Mode	Dir X	Dir Y
1	0%	53%
2	0%	16%
3	70%	0%
4	3%	0%

Period [s]

Mode	T_{num}	T_{exp}
1	0.293	0.297
2	0.286	0.278
3	0.226	0.225
4	0.191	0.204

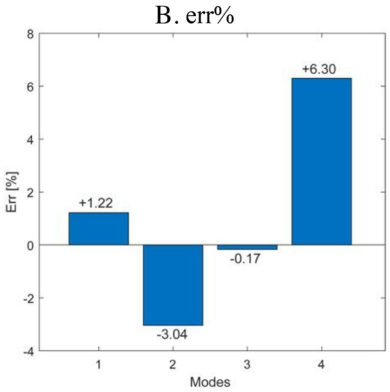

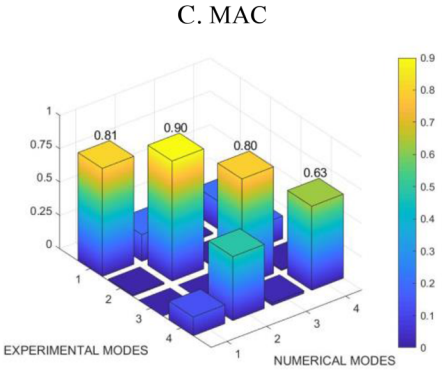

FIGURE 14 Final model resulting from the calibration process: (A) participant masses and experimental and numerical periods for the first four modes, (B) error per cent, and (C) modal assurance criterion (MAC) index

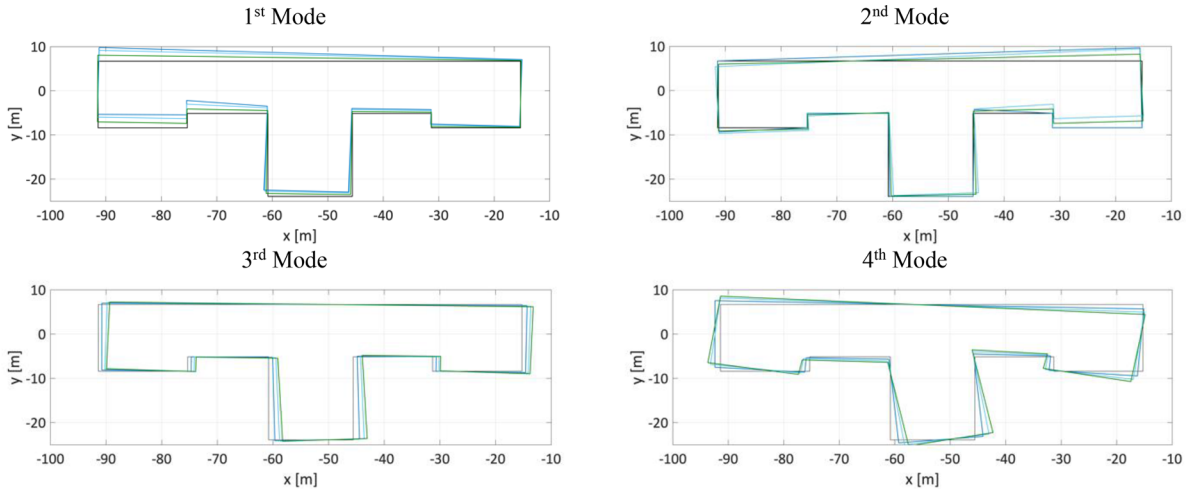

FIGURE 15 Mode shapes of the calibrated numerical model

5 | VALIDATION OF THE EQUIVALENT FRAME MODEL IN NONLINEAR FIELD

The validation of the calibrated model in the nonlinear field is described hereinafter by simulating the dynamic response of the structure during the shock of October 26, 2016 (19:18 earthquake). NLDA were performed by using the three components of the accelerogram (recorded by the monitoring system at the base of the building, that is, sensors no. 29, 30, and 31 of Figure 4A) as input. To perform the NLDA, the following assumptions were made:

- The nonlinear response of panels was modelled by adopting the piecewise-linear constitutive laws formulated by Cattari et al.[50] and implemented in the research version of the software package Tremuri.[21,51] Such constitutive laws are based on a phenomenological approach. They are able to simulate the nonlinear response through progressive strength degradation in correspondence with assigned drift values and to describe different hysteretic responses.
- A Rayleigh damping was introduced. The damping coefficient was set to 3% in the range of the following conventional periods: the first period of the modal analysis (T_1) and the secant period (T_{sec}) computed by assuming a ductility value of 4 (i.e., $T_{sec} = 2T_1$). The latter allows to take into account the evolution in the nonlinear range of the structural response and to avoid excessive overestimations of the visco-elastic damping during nonlinear dynamic analyses.

Concerning the strength mechanical parameters, Table 7 presents the assumed values, differentiated for piers and spandrels. The latter was defined on the basis of the results from the sensitivity analyses, starting from the reference values proposed in the Italian Technical Code[47] and choosing the minimum or maximum value coherent to the assumed value for the elastic stiffness parameters after calibration.

TABLE 7 Mechanical properties assumed for piers and spandrels

		Piers					Spandrels				
(N/cm²)		$X_1 = X_{11}$	$X_2 = X_{13}$	$X_3 = X_{12}$	X_4	X_5	$X_6 = X_{16}$	$X_7 = X_{14}$	$X_8 = X_{15}$	X_9	X_{10}
Numerical model	f_m	593	593	900	254	606	494	593	593	900	600
	τ_0	11.5	11.5	20.7	5.7	12.7	9.6	11.5	11.5	20.7	13.8

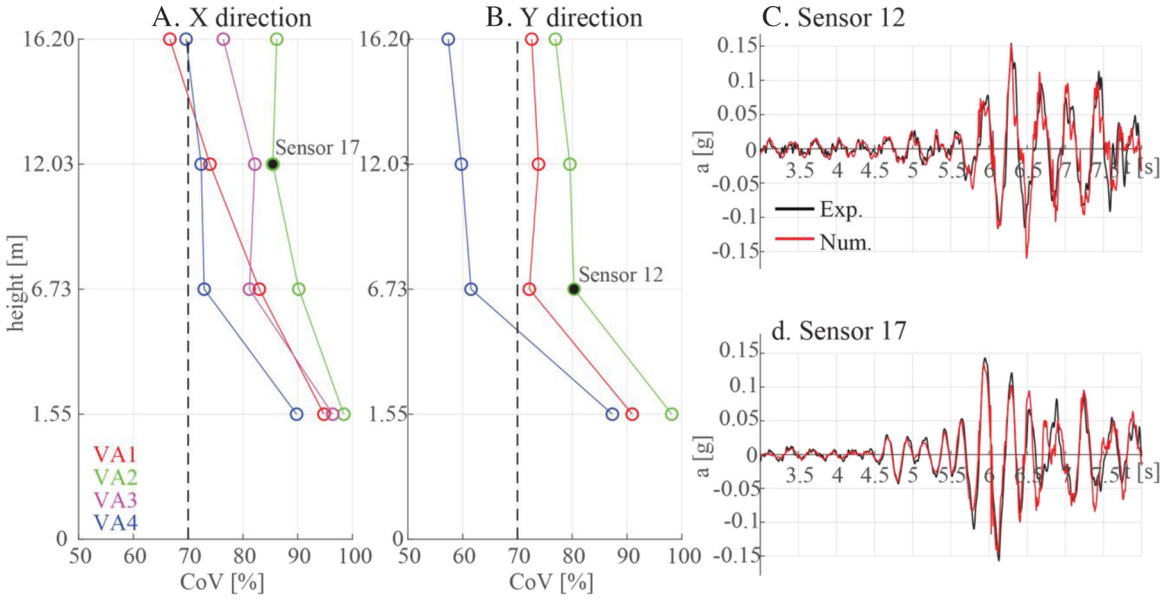

FIGURE 16 Comparison of numerical and experimental accelerations (sensors are placed as in Figure 4A)

The maximum shear strength of masonry panels modelled as nonlinear beams were computed according to a simplified analytical strength criterion. A detailed review is presented in Calderini et al.,[52] for piers, and in Beyer and Mangalathu,[53] for spandrels, respectively. More specifically, the shear failure mode was described by referring to the diagonal shear cracking classified according to the criterion proposed in Turnsek and Sheppard[54] and based on the use of the shear strength τ_0. The flexural response was assigned to piers through the common criterion proposed in Codes,[55,56] neglecting the tensile strength of the material and assuming a stress block of normal distribution at the compressed toe. Conversely, in the case of spandrels, the flexural response was also interpreted to account for the contribution of equivalent tensile strength.[47,53] The latter is justified by the interlocking phenomena that may be activated at the end sections, favoured in the former Courthouse in Fabriano by the strengthening interventions realized (reinforced plaster). Finally, with regards to the other parameters in defining the constitutive law, the assumed drift was consistent with those proposed in technical literature[57] and supported by experimental evidence from existing masonry typologies.[1,48] Concerning the hysteretic response, values compatible with those already described in Cattari et al.[51] were adopted for the coefficients which control the unloading and uploading phases.

Although it is evident that strength parameters are also affected by uncertainties, in the numerical simulation they were considered as deterministic. This choice is consistent with a blind prediction that a common and expert analyst would perform, first, calibrating the model against the dynamic identification data from AVTs and, then, by defining all the other parameters through expert judgment. Indeed, the valuable data from permanent monitoring and recordings from seismic events are usually missing in common engineering applications.

Figures 16 and 17 present the comparison between the experimental and numerical results, initially provided at a local scale. In particular, Figure 16 shows: the covariance (CoV) between experimental and numerical accelerations obtained from the sensors placed along the same Vertical Alignment (VA) identified in Figure 4A (Figures 16A and B); the comparison between the experimental (in black) and numerical (in red) acceleration time histories for the two sensors no. 12 and 17 (Figures 16C and D). In contrast, Figure 17 illustrates the comparison between experimental (continuous graphs) and numerical (dashed graphs) acceleration floor spectra obtained from the sensors placed along the same VAs. The results indicate a sufficient correlation between numerical and experimental data, being that the CoV coefficients are in general

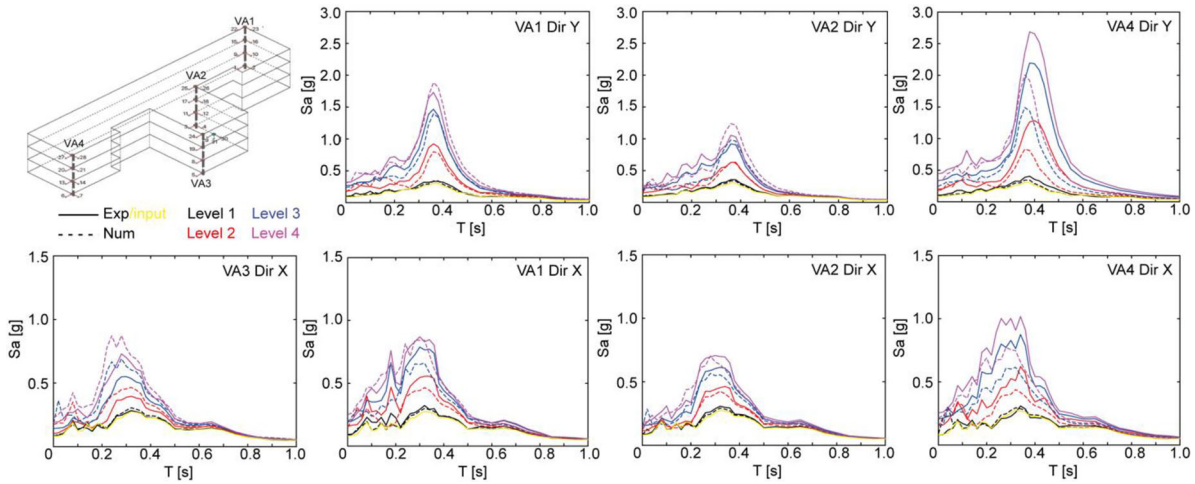

FIGURE 17 Comparison between numerical and experimental acceleration spectra

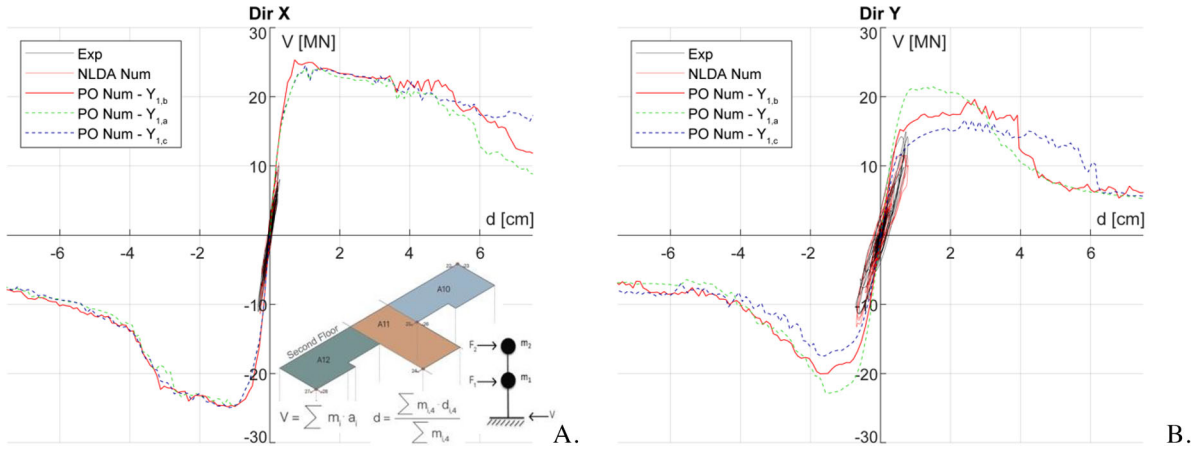

FIGURE 18 Comparison between the experimental and numerical *V-d* curve evaluated from NLDA in the (A) X and (B) Y directions. Also, the pushover curves (PO) obtained from NLSA under the three modelling strategies considered for the flange effect (namely Y_1) are reported

higher than 70, except for the VA4 in the Y direction (with values around 60%). Moreover, from Figure 17, it is possible to observe that the numerical model is able to correctly reproduce the amplification phenomena on the seismic action provided by the filtering effect of the structure. A favourable agreement was observed for all sensors except for those in VA4, in which a slight underestimation was noticed as already highlighted. Validating the capability of models to reproduce such phenomena is extremely valuable from an engineering point of view. That is due to the fact that the numerical model constitutes the tool for seismic assessment in both structural and non-structural components.[58]

Furthermore, the comparison was intensified by checking the entities representative of the global response. Figure 18 shows the results in terms of dynamic hysteretic curves "inertial forces *V versus* top displacement *d*". The experimental curve (plotted in black in the figure) was evaluated by defining an equivalent M-DOF system (where *M* is equal to the number of stories) and by computing *V* as the sum of the product of the experimentally recorded accelerations (a_i) and the corresponding masses (m_i). The latter was estimated on the basis of the conventional area attributed to each sensor as illustrated in Figure 18A. The top displacement *d* was computed as the average displacement of nodes on the top level, weighted on the pertinent mass.

Together with the results of NLDA, Figure 18 also shows the results of the NLSA performed by the assumption that the load pattern was proportional to the masses (PO in the figure). In particular, the different pushover curves correspond to the different alternatives discussed in Section 4.3.1 for the flange effect (Y_1). Although, the most reliable option for the examined case was b. In addition, the others are discussed here in order to show how this factor can significantly affect

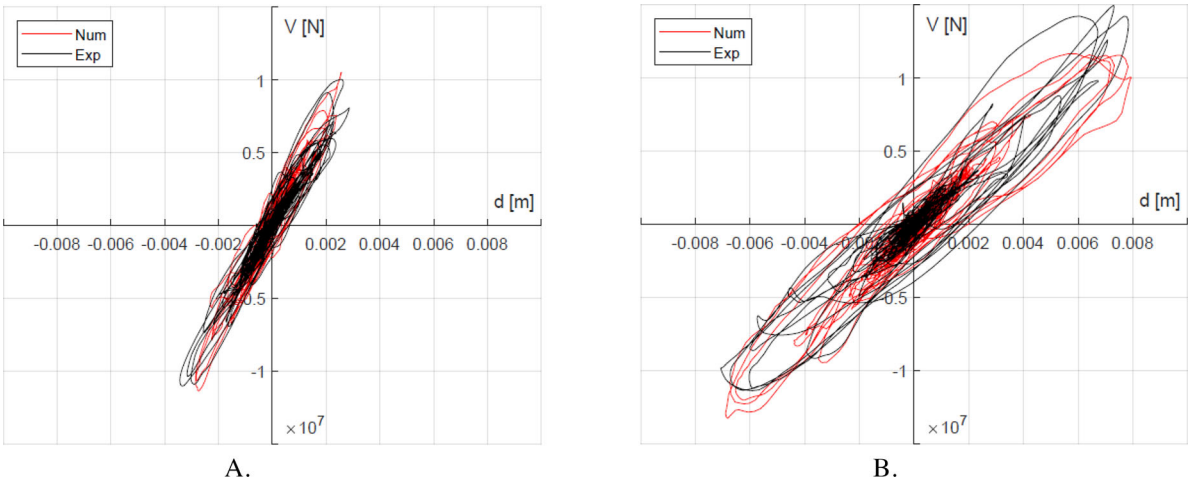

FIGURE 19 *V-d* hysteretic curve from NLDA: comparison between experimental and numerical results in (A) X and (B) Y directions

the structural response in the nonlinear phase. The results show the effects of varying the stiffness of the equivalent beam which is modelled to simulate the flange effect (namely Y_1 a, b or c). In fact, a noticeable variation in both the overall base shear and ductility, particularly in the *Y* direction, is observed. This is consistent with the presence of many internal walls which are orientated in this direction with few or no openings. This result supports how useful AVTs are in addressing modelling choices that affect not only the linear but also the nonlinear response. This is especially evident when the structure is subjected to seismic actions.

Figure 18 also highlights that the structural response is in the pseudo-elastic field (visible by comparing the hysteretic with the pushover curves); the latter result is consistent with the damage survey which showed negligible damage to the structure. Finally, Figure 19 shows a close-up of the hysteretic curves which confirms that the numerical results (in red) fit very well within the experimental ones (in black).

6 | CONCLUSIONS

The results presented in this paper highlight the significant benefit of having data from both ambient vibration tests and seismic monitoring. In fact, AVT signals allowed for the proper calibration of the dynamic response in the elastic field, while strong motion data were used to validate the structural response in the nonlinear range.

The studied URM building is interesting because of (i) its architectural features (similar applications, available in the literature, involved only towers and churches); (ii) its complexity, which causes the calibration process to be much more challenging; and (iii) the availability of recordings during earthquakes, which are essential to validate the numerical model and for its use as a more reliable seismic assessment.

Modal dynamic identification performed using various techniques allowed for the extraction of natural frequencies and mode shapes, while also assessing the reliability of the obtained results. Among the employed techniques, the pLSCF and the SSI-Cov ones proved to be particularly effective. The extraction of modal parameters, using seismic monitoring data, highlighted the tendency of frequencies to decrease as earthquake intensity and amplitude increases. As confirmed by the evidence gathered on the actual response of the structure, variations are not due to the activation of irreversible nonlinear behaviour of the structure (associated with seismic damage), but it may depend on reversible, amplitude-dependent nonlinearities inherent in the system's response. This wandering of modal parameters has to be taken into account when interpreting seismic monitoring data.

The model calibration in the elastic field highlighted the potential of the sensitivity analysis to better understand those uncertainties that affect the building response most. Moreover, it underlined the importance of AVTs data as a target for calibration allowing us to address the appropriate strategy for the alternative options considered. AVTs data turn out particularly effective in the cases when local inspections are problematic and often inconclusive, for example, wall-to-wall connections. These results – together with the technological advancements of the last few decades and the associated costs becoming more convenient – suggest that the use of dynamic monitoring is a very efficient resource with minimum impact on the structure. As clarified in this paper, the Central Italy earthquake sequence caused only slight damage to the

structure. Therefore, this case study, in contrast with others,[18] is not considered to be the ideal example for a solid validation in the strong nonlinear phase. Nevertheless, the achieved results provided valuable outcomes from an engineering point of view. For example, the comparison between the actual and numerical response showed that the calibrated model was able to properly describe the amplification phenomena of the seismic input. The capability of the model to simulate the latter phenomenon is very useful for the verification of non-structural components or, in case of URM structures, of local mechanisms associated with the out-of-plane response.

In conclusion, the validation of the calibrated model confirmed the potential of the selected modelling strategy. The equivalent frame approach demonstrated in fact to perform very well in simulating the seismic response of existing complex masonry buildings, at least when a box-like behaviour type is guaranteed, as in this case.

ACKNOWLEDGMENTS

The results presented in this paper have been obtained within the ReLUIS Project 2019–2021 (WP6) and benefitted from the data made available by the Italian structural seismic monitoring network (OSS) of the Italian Department of Civil Protection within the research activities of the ReLUIS Project 2017–2018 (WP4.1).

ORCID

Serena Cattari https://orcid.org/0000-0001-9459-5989
Stefania Degli Abbati https://orcid.org/0000-0001-9991-8599
Andrea Brunelli https://orcid.org/0000-0002-5505-1521
Filippo Lorenzoni https://orcid.org/0000-0003-1195-702X
Francesca da Porto https://orcid.org/0000-0002-9346-9902

REFERENCES

1. Krzan M, Gostic S, Cattari S, Bosiljkov V. Acquiring reference parameters of masonry for the structural performance analysis of historical building. *Bull Earthq Eng*. 2015;13(1):203-236.
2. Sivori D, Lepidi M, Cattari S. Structural identification of the dynamic behavior of floor diaphragms in existing buildings. *Smart Struct Syst*. 2021;27(2):173-191.
3. Snoj J, Österreicher M, Dolšek M. The importance of ambient and forced vibration measurements for the results of seismic performance assessment of buildings obtained by using a simplified non-linear procedure: case study of an old masonry building. *Bull Earthq Eng*. 2013;11(6):2105-2132.
4. Clotaire M, Guéguen P, Bard PY. Dynamic parameters of structures extracted from ambient vibration measurements: an aid for the seismic vulnerability assessment of existing buildings in moderate seismic hazard regions. *Soil Dyn Earthq Eng*. 2008;28(8):593-604.
5. Tecchio G, Lorenzoni F, Caldon M, Donà M, da Porto F, Modena C. Monitoring of orthotropic steel decks for experimental evaluation of residual fatigue life. *J Civil Struct Health Monit*. 2017;7:517-539.
6. Lorenzoni F, De Conto N, da Porto F, Modena C. Ambient and free-vibration tests to improve the quantification and estimation of modal parameters in existing bridges. *J Civil Struct Health Monit*. 2019;9(5):617-637.
7. Karatzetzou A, Negulescu C, Manakou M, et al. Ambient vibration measurements on monuments in the Medieval City of Rhodes, Greece. *Bull Earth Eng*. 2015;13(1):331-345.
8. Gattulli V, Lepidi M, Potenza F. Dynamic testing and health monitoring of historic and modern civil structures in Italy. *Struct Monit Maint*. 2016;3(1):71-90.
9. Modena C, Lorenzoni F, Caldon M, da Porto F. Structural health monitoring: a tool for managing risks in sub-standard conditions. *J Civil Struct Health Monit*. 2016;6(3):365-375.
10. Masciotta MG, Ramos LF, Lourenço PB. The importance of structural monitoring as a diagnosis and control tool in the restoration process of heritage structures: a case study in Portugal. *J Cult Herit*. 2017;27:36-47.
11. Gentile C, Saisi A. Ambient vibration testing of historic masonry towers for structural identification and damage assessment. *Constr Build Mater*. 2007;21(6):1311-1321.
12. Ramos LF, Marques L, Lourenço PB, De Roeck G, Campos-Costa A, Roque J. Monitoring historical masonry structures with operational modal analysis: two case studies. *Mech Syst Signal Pr*. 2010;24(5):1291-1305.
13. Foti D, Diaferio M, Giannoccaro NI, Mongelli M. Ambient vibration testing, dynamic identification and model updating of a historic tower. *NDT&E Int*. 2012;47:88-95.
14. Pierdicca A, Clementi F, Isidori D, Concettoni E, Cristalli C, Lenci S. Numerical model upgrading of a historical masonry palace monitored with a wireless sensor network. *IJMRI*. 2016;1(1):74-98.
15. Saisi A, Gentile C, Guidobaldi M. Post-earthquake continuous dynamic monitoring of the Gabbia Tower in Mantua, Italy. *Constr Build Mater*. 2015;81:101-112.
16. Ubertini F, Cavalagli N, Kita A, Comanducci G. Assessment of a monumental masonry bell-tower after 2016 central Italy seismic sequence by long-term SHM. *Bull Earthq Eng*. 2018;16(2):775-801.

17. Gentile C, Ruccolo A, Saisi A. Continuous dynamic monitoring to enhance the knowledge of a historic bell-tower. *Int J Archit Herit*. 2019;13:992-1004.
18. Brunelli A, de Silva F, Piro A, et al. Numerical simulation of the seismic response and soil-structure interaction for a monitored masonry school building damaged by the 2016 Central Italy earthquake. *Bull Earthq Eng*. 2021;19(2):1181-1211.
19. Dolce M, Nicoletti M, De Sortis A, Marchesini S, Spina D, Talanas F. Osservatorio sismico delle strutture: the Italian structural seismic monitoring network. *Bull Earthq Eng*. 2017;15:621-641.
20. Cattari S, Degli Abbati S, Ottonelli D, et al. Discussion on data recorded by the Italian structural seismic monitoring network on three masonry structures hit by the 2016–2017 central Italy earthquake. COMPDYN 2019. 24–26 June 2019; Crete, Greece.
21. Lagomarsino S, Penna A, Galasco A, Cattari S. TREMURI program: an equivalent frame model for the nonlinear seismic analysis of masonry buildings. *Eng Struct*. 2013;56:1787-1799.
22. EC (Eurocode) 8. *Design of Structures for Earthquake Resistance – Part 1: General Rules, Seismic Actions and Rules for Buildings*. Brussels, Belgium: CEN; 2004.
23. Brincker R, Zhang L, Andersen P. *Modal identification from ambient response using frequency domain decomposition*. In: Proceedings from the International Society for Optical Engineering; February 7–10, 2000; San Antonio, TX. 625-630.
24. Brincker R, Ventura CE, Andersen P. *Damping estimation by frequency domain decomposition*. In: Proceedings of IMAC 19: A Conference on Structural Dynamics; February 5–8, 2001; Kissimmee, Fl. 698-703.
25. Guillaume P, Verboven P, Vanlanduit S, Van der Auweraer H, Peeters B. *A poly-reference implementation of the least-squares complex frequency-domain estimator*. February 5–8, 2003; Kissimmee, Fl. 1-9.
26. Megalhaes F, Cunha A. Explaining operational modal analysis with data from an arch bridge. *Mech Syst Signal Pr*. 2011;25:1431-1450.
27. Peeters B, De Roeck G. Stochastic system identification for operational modal analysis: a review. *J Dyn Sys Meas Control*. 2001;123(4):659-667.
28. Reynders E, De Roeck G. Reference-based combined deterministic–Stochastic subspace identification for experimental and operational modal analysis. *Mech Syst Signal Pr*;22(3):617-637.
29. Allemange RJ, Brown DL. A correlation coefficient for modal vector analysis. In: Proceedings of the1st international modal analysis conference; November 8–10, 1982; Orlando, Fl. 110-116.
30. Ceravolo R, Matta E, Quattrone A, Zanotti Fragonara L. Amplitude dependence of equivalent modal parameters in monitored buildings during earthquake swarms. *Earthquake Engng Struct Dyn*. 2017;46:2399-2417.
31. Clinton J. The observed wander of the natural frequencies in a structure. *Seismol Soc Am Bull*. 2006;96(1):237-257.
32. Celebi M. On the variation of fundamental frequency (period) of an undamaged building—a continuing discussion. In: Proceedings of the Conference on Experimental Vibration Analysis for Civil Engineering Structures; October 24–26, 2007; Porto, Portugal. 317-326.
33. Lorenzoni F, Casarin F, Modena C, Caldon M, Islami K, da Porto F. Structural health monitoring of the Roman Arena of Verona, Italy. *J Civil Struct Health Monit*. 2013;3(4):227-246.
34. Sehgal S, Harmesh K. Structural dynamic model updating techniques: a state of the art. *Arch Computat Methods Eng*. 2016;23:515-533.
35. Ewins DJ. *Modal Testing: Theory, Practice and Application*. Baldock, England: Research Studies Press Ltd; 2000.
36. Jaishi B, Ren WX. Structural finite element model updating using ambient vibration test results. *J Struct Eng*. 2005;131(4):617-628.
37. Haddad J, Cattari S, Lagomarsino S. Use of the model parameter sensitivity analysis for the probabilistic-based seismic assessment of existing buildings. *Bull Earthq Eng*. 2019;17:1983-2009.
38. 3Muri [program]. Release 11.5.7. Torino TO, Italy: S.T.A. Data; 2018. https://www.3muri.com.
39. Augenti N. Seismic behavior of irregular masonry walls. In: Proceedings of the 1st European Conference on Earthquake Engineering and Seismology; 3–8 September, 2006; Geneva, Switzerland.
40. Dolce M. Schematizzazione e modellazione degli edifici in muratura soggetti ad azioni simiche. *L'industria delle costruzioni*. 1991;25(242):44-57. [In Italian].
41. Moon FL, Yi T, Leon RT, Kahn LF. Recommendations for seismic evaluation and retrofit of low-rise URM structures. *J Struct Eng*. 2006;132(5):663-672.
42. Cattari S, Camilletti D, D'Altri AM, Lagomarsino S. On the use of continuum Finite Element and Equivalent Frame models for the seismic assessment of masonry walls. *J Build Eng*. 2021;43 https://doi.org/10.1016/j.jobe.2021.102519.
43. Ottonelli D, Manzini CF, Marano C, Cordasco EA, Cattari S. A comparative study on a complex URM building: part I—sensitivity of the seismic response to different modelling options in the equivalent frame models. *Bull Earthq Eng*. 2021; https://doi.org/10.1007/s10518-021-01128-7.
44. Ferrero C, Lourenco PB, Calderini C. Nonlinear modeling of unreinforced masonry structures under seismic actions: validation using a building hit by the 2016 Central Italy earthquake. *Frattura Integr Strutt*. 2020;14(51):92-114.
45. Gazetas G. Formulas and charts for impedances of surface and embedded foundations. *J Geotech Eng*. 1991;117(9):1363-1381.
46. Maravas A, Mylonakis G, Karabalis DL. Simplified discrete systems for dynamic analysis of structures on footings and piles. *Soil Dyn Earthq Eng*. 2014;61-62:29-39.
47. Ministry of Infrastructures and Transportation. Circular n. 7 CSLL.PP. - Instructions for the application of the update of the - Technical standards for constructions referred to in the ministerial decree of 17 January 2018. January 21, 2019. Ministry of Infrastructures and Transportation; G.U. S.O. n.35 of 11/2/2019. [In Italian].
48. Vanin F, Zaganelli D, Penna A, Beyer K. Estimates for the stiffness, strength and drift capacity of stone masonry walls based on 123 quasi-static cyclic tests reported in the literature. *Bull Earthq Eng*. 2017;15(12):5435-5479.

49. CEN. Eurocode 6: Design of masonry structures, Part 1: General rules for reinforced and unreinforced masonry structures. EN 1996-1-1. November 2005. Comité Européen de Normalisation, Brussels.
50. Cattari S, Lagomarsino S. Masonry structures. In: Sullivan T and Calvi GM, eds. *Developments in the Field of Displacement based Seismic Assessment*. Pavia, Italy: IUSS Press; 2013:151-200.
51. Cattari S, Camilletti D, Lagomarsino S, Bracchi S, Rota M, Penna A. Masonry Italian code-conforming buildings. Part 2: nonlinear modelling and time-history analysis. *JEarthqEng*. 2018;22(sup2):2010-2040.
52. Calderini C, Cattari S, Lagomarsino S. In-plane strength of unreinforced masonry piers. *Earthquake Engng Struct Dyn*. 2009;38:243-267.
53. Beyer K, Mangalathu S. Review of strength models for masonry spandrels. *Bull Earthq Eng*. 2013;11(2):521-542.
54. Turnsek V, Sheppard P. The shear and flexural resistance of masonry walls. In: Proceedings of the International Research Conference on Earthquake Engineering; June 30– July 3, 1980; Skopje, Macedonia.
55. NTC. Italian Technical Code, Decreto Ministeriale 17/1/2018. "Aggiornamento delle Norme tecniche per le costruzioni". 2018. Ministry of Infrastructures and Transportation; G.U. n.42 of 20/2/2018 (In Italian).
56. EN1998 – 3. Eurocode 8: design of structures for earthquake resistance – Part 3: assessment and retrofitting of buildings. 2005. Comité Européen de Normalisation.
57. CNR-DT 212/2013. *Guide for the Probabilistic Assessment of Seismic Safety of Existing Buildings*. Rome, Italy: National Research Council of Italy; 2014.
58. Degli Abbati S, Cattari S, Lagomarsino S. Theoretically-based and practice-oriented formulations for the floor spectra evaluation. *Earthq Struct.*. 2018;15(5):565-581.

How to cite this article: Cattari S, Degli Abbati S, Alfano S, Brunelli A, Lorenzoni F, da Porto F. Dynamic calibration and seismic validation of numerical models of URM buildings through permanent monitoring data. *Earthquake Engng Struct Dyn*. 2021;1–22. https://doi.org/10.1002/eqe.3467